Stokes Localized Structure in Kerr Resonators

Mulong Liu,[1] Huimin Huang,[2,*] Zhizhou Lu,[3,†] Yaai Dang,[1] Sen Mei,[1] Chang Wang,[1] Bailing Zhao,[3] and Wei Zhao[4]

[1]*School of Science, Northwest A&F University, Yangling 712100, China*

[2]*College of Information Engineering, Northwest A&F University, Yangling 712100, China*

[3]*Chongqing United Microelectronics Center (CUMEC), Xiyuan South Street, Chongqing 401332, China*

[4]*State Key Laboratory of Transient Optics and Photonics, Xi'an Institute of Optics and Precision Mechanics (XIOPM), Chinese Academy of Sciences (CAS), Xi'an 710119, China*

We theoretically demonstrate generation of the Stokes temporal localized structure (TLS) by exploiting its Raman interaction in space and time within an optical potential well shared with another dark pulse. Excitation of the Stokes TLSs is feasible in both the normal and anomalous group-velocity dispersion regime, with a single modulated pump source. Stimulated Raman scattering constitutes influences on the stability and physical feature of the generated Stokes TLS (STLS). Particularly, breathing STLSs are also observed due to the periodic energy transfer between the primary and the Stokes fields. These findings could deepen the understanding of complex nonlinear dynamics in resonators and facilitate the excitation of different types of TLSs in potential platforms.

I. INTRODUCTION

Temporal localized structures (TLSs) are coherent pulses of light that can circulate indefinitely in dissipative Kerr resonators, usually classified as dark pulses or bright solitons existing in the normal and anomalous group-velocity dispersion (GVD) regime, respectively [1]. Their shapes exhibit extremely stable characteristics thanks to compensation of dispersion and Kerr nonlinear effects [2]. They have been observed in macroscopic fiber ring cavities [3] and monolithic microresonators [4–9], where they play an extraordinary role in the generation and application of low-noise, broadband optical frequency combs. Frequency comb generation in microresonators has witnessed tremendous progress, facilitating emergent applications in astronomy [10,11], metrology [12–15], spectroscopy [16–18], and optoelectronic oscillator [19].

In addition to the Kerr nonlinearity, another effect associated with TLS properties is the stimulated Raman scattering (SRS), which introduces a redshift of the soliton spectrum in microcavities [20], also termed as Raman self-frequency shift (RSFS). Such a phenomenon exists in amorphous materials (e.g., Si_3N_4 [21] and SiO_2 [22]), where the Raman gain bandwidth is much larger than the cavity free-spectral range (FSR). Crystalline materials (e.g., $LiNbO_3$ [23] and AlN [8,24]) with narrow and

strong Raman gain also exhibit RSFS, even if the gain bandwidth is narrower than the resonator FSR. Furthermore, Raman gain can produce optical amplification and laser action of waves with redshifted wavelength relative to a pump pulse [25]. Recently, Raman-related effects have been reported, the bright Stokes soliton generation through Raman amplification created by the pump soliton [26,27]. SRS is also found to impose a fundamental limit on the duration and bandwidth of bright solitons in the anomalous GVD regime [3]. In normal dispersion platforms, there is competition between SRS and Kerr effects [28,29]. SRS may not only stablize moving bright localized structures [30], but also has implications on the bifurcation structure [31] and stability of the localized structures [29]. Yet, the specific pattern in which SRS affects the emission and stability of TLS in the normal GVD regime has not to date been thoroughly revealed.

Excitation of the Stokes TLS in the normal GVD theoretically requires that the longitudinal modes of the Stokes field are located within the Raman gain spectrum created by the primary dark pulse on the one hand, and the Stokes field can overlap in space and time with the primary dark pulse when they circulate in the resonators on the other. Once the Raman gain from the pump field is sufficient to balance the total cavity loss, any noise will be amplified and parametric oscillation is possible [26,27]. The overlap of two fields could be destroyed due to their different group velocity related to overall dispersion.

---

*huanghm@nwafu.edu.cn

†zhizhou.lu@cumec.cn

Temporal drift between two pulses in cavity associated with high-order dispersion and RSFS can be restrained by the potential well caused by the modulated driving field.

In this work, we investigate the STLS generation via the Raman gain from a dark pulse formed by the pump amplitude modulation in the normal GVD region. Both the Stokes dark pulse and the Stokes solitonlike temporal structures can be initiated in the normal and anomalous GVD regime, respectively. The repetition frequency of both the initial and the Stokes TLS are locked by the modulation frequency, suppressing the RSFS and matching the above mentioned conditions. The influences of SRS on the stability and physical feature of intracavity STLS have also been discussed. In particular, breathing dynamics are also observed due to the energy transfer between the pump and the Stokes fields. Reported findings provide deep insight into the complex dynamics of the SRS processes in Kerr resonators.

II. THEORETICAL MODEL

We start by briefly introducing the physical process as shown in Fig. 1. An amplitude-modulated pump is injected into a Kerr resonator with normal GVD to obtain the primary pulse (the blue particle). The energy of the primary pulse can be transferred to the Stokes pulse (the red particle) via the nonlinear Raman gain. Such a nonlinear process can be theoretically described using the coupled mean-field Lugiato-Lefever equation (LLE). The interaction between two pulses via cross-phase-modulation and the SRS process has been previously studied in optical fibers using coupled-pulse-propagation equations [32]. Such a model can be extended to investigate the Stokes localized structure in Kerr resonators [26]. The coupled equations describing the intracavity's slowly varying field amplitudes for the primary and the Stokes pulse system can be adapted from the LLE augmented by Raman interactions [26,33],

$$
T_R \frac{\partial E_p(t,\tau)}{\partial t} = -\alpha_p E_p - i\delta_p E_p + iL \sum_{n\geq 2} \frac{\beta_{pn}}{n!} \left(i\frac{\partial}{\partial\tau}\right)^n E_p
$$

$$
+ i\gamma_p L (1 - f_R) \left(|E_p|^2 + 2|E_s|^2\right) E_p
$$

$$
+ i f_R \gamma_p L E_p \int h_R(\tau') \left(|E_p(\tau - \tau')|^2\right.
$$

$$
\left. + |E_s(\tau - \tau')|^2\right) d\tau'
$$

$$
+ i f_R \gamma_p L E_s \int h_R(\tau') E_p E_s^* \exp(i\Omega\tau') d\tau'
$$

$$
+ \sqrt{\kappa} E_{\text{in}}, \tag{1}
$$

$$
T_R \frac{\partial E_s(t,\tau)}{\partial t} = -\alpha_s E_s - i\delta_s E_s + iL \sum_{n\geq 2} \frac{\beta_{sn}}{n!} \left(i\frac{\partial}{\partial\tau}\right)^n E_s
$$

$$
- \sigma \frac{\partial E_s}{\partial\tau} + i\gamma_s L (1 - f_R) \left(|E_s|^2 + 2|E_p|^2\right) E_s
$$

$$
+ i f_R \gamma_s L E_s \int h_R(\tau') \left(|E_p(\tau - \tau')|^2\right.
$$

$$
\left. + |E_s(\tau - \tau')|^2\right) d\tau'
$$

$$
+ i f_R \gamma_s L E_p \int h_R(\tau') E_s E_p^* \exp(-i\Omega\tau') d\tau', \tag{2}
$$

$$
h_R(\tau) = \frac{\tau_1^2 + \tau_2^2}{\tau_1 \tau_2^2} \exp\left(-\frac{\tau}{\tau_2}\right) \sin\left(\frac{\tau}{\tau_1}\right), \tag{3}
$$

where $\alpha_{p,s}$, $E_{p,s}$, $\delta_{p,s}$, $\beta_{pn,sn}$, $\gamma_{p,s}$, are the total round-trip loss coefficient, field amplitude, detuning, nth-order dispersion coefficient, Kerr nonlinear coefficient of the pump and the Stokes field, respectively. L, T_R, τ, T, E_{in}, and f_R denote cavity perimeter length, round-trip time, fast time, slow time, pump amplitude, and Raman fraction, respectively. The Kerr nonlinear coefficient $\gamma_{p,s} = n_2 \, \omega_{p0,s0}/cA_{\text{effp,effs}}$ with $A_{\text{effp,effs}}$, $\omega_{p0,s0}$, and n_2 representing the effective mode area, angular frequency, and nonlinear refractive index of the pump and Stokes pulses, respectively. σ is the FSR difference between the primary and Stokes pulses. The kernel or influence function $h_R(\tau)$ is the nonlocal delay response term modeling the SRS. The parameters $\tau_{1,2}$ depend on the type of medium. We focus on the common parameters of fused silica with $f_R = 0.18$, $\tau_1 = 12.2$ fs, and $\tau_2 = 32$ fs. There is a Raman shift between the carrier frequency of pump and Stokes pulses, thus the relationship of group-velocity dispersion, nonlinear coefficient, and Raman gain between the pump field and Stokes pulse can be expressed as

$$
\beta_{s2} = \frac{\lambda_p}{\lambda_s} \beta_{p2}, \gamma_s = \frac{\lambda_p}{\lambda_s} \gamma_p. \tag{4}
$$

Generally, the pulse width in our considered system is several hundred femtosecond, which is much longer than the Raman response time (approximately 10 fs), thus the pulse fields $E_{p,s}$ can be considered slowly varying variables when compared with $h_R(\tau)$. Therefore, the last terms in Eqs. (1) and (2) associated with Raman response function can be expanded into a Taylor series written as

$$
E_k \int h_R(\tau') E_j E_k^* \exp(\pm i\Omega\tau') d\tau'
$$

$$
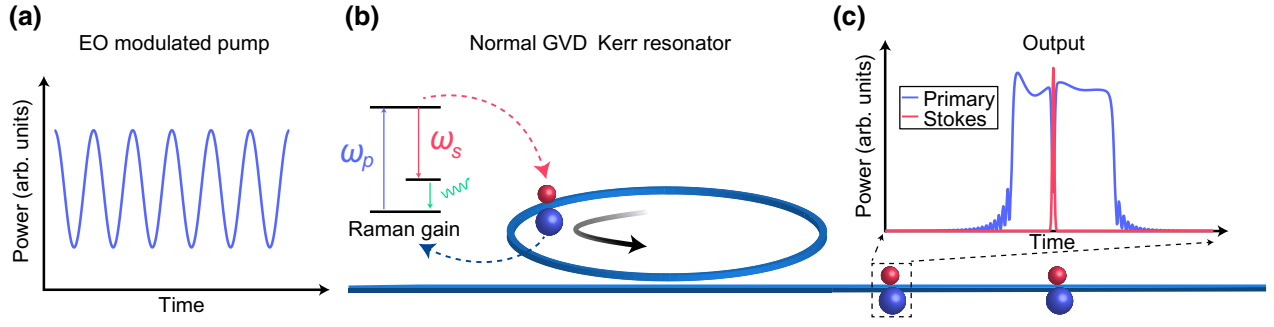\approx |E_k|^2 E_j \int h_R(\tau') \exp(\pm i\Omega\tau') d\tau', \tag{5}
$$

FIG. 1. Schematic process of STLS generation. (a) Amplitude-modulated pump source. (b) Primary pulse (the blue particle) formation via pump modulation and the Stokes pulse (the red particle) excitation with the nonlinear Raman gain in cavity. (c) Output locked pulse profile.

For generalization, Eqs. (1)–(5) can be normalized and written in the dimensionless form,

$$\frac{\partial \psi_p}{\partial \zeta} = -\left(1 + i\Delta_p\right)\psi_p - i\frac{d_{p2}}{2}\frac{\partial^2 \psi_p}{\partial \eta^2} + i\sum_{n\geq 3}\frac{d_{pn}}{n!}\frac{\partial^n \psi_p}{\partial \eta^n}$$

$$+ i\left(1 - f_R\right)\left(\left|\psi_p\right|^2 + 2\left|\psi_s\right|^2\right)\psi_p$$

$$+ if_R\left(\Re \otimes \left(\left|\psi_p\right|^2 + \left|\psi_s\right|^2\right)\right)\psi_p - G_R\left|\psi_s\right|^2\psi_p$$

$$+ F(1 + l\cos\Omega\eta), \tag{6}$$

$$\frac{\partial \psi_s}{\partial \zeta} = -\left(1 + i\Delta_s\right)\psi_s - \sigma\frac{\partial \psi_s}{\partial \eta} - ir\frac{d_{s2}}{2}\frac{\partial^2 \psi_s}{\partial \eta^2}$$

$$+ i\sum_{n\geq 3}\frac{d_{sn}}{n!}\frac{\partial^n \psi_s}{\partial \eta^n} + ir\left(1 - f_R\right)\left(\left|\psi_s\right|^2 + 2\left|\psi_p\right|^2\right)\psi_s$$

$$+ irf_R\left(\Re \otimes \left(\left|\psi_p\right|^2 + \left|\psi_s\right|^2\right)\right)\psi_s + rG_R\left|\psi_p\right|^2\psi_s, \tag{7}$$

$$\Re(\eta) = H(\eta) \bullet ae^{-b\eta}\sin(c\eta), \tag{8}$$

$$G_R = \frac{2abc\omega}{\left(a^2 + b^2 - \omega^2\right)^2 + 4a^2\omega^2}, \tag{9}$$

where we assume $\alpha = \alpha_p = \alpha_s$. The parameters follow $\psi_{p,s} = E_{p,s}/\sqrt{\alpha/\gamma_{p,s}L}$, $\zeta = t\alpha/T_R$, $\eta = \tau\sqrt{\alpha/|\beta_2|L}$, $\Delta_{p,s} = \delta_{p,s}/\alpha$, $d_{pn,sn} = i^{n+1}\left(\alpha/L\right)^{n/2-1}\beta_{pn,sn}/|\beta_2|^{n/2}$, $F = E_{in}\sqrt{\kappa\gamma_p L/\alpha^3}$, $r = \lambda_p/\lambda_s$. Ω is the pump modulation frequency and l is the modulation depth. $d_{p2,s2} = \pm 1$ refers to the normal or anomalous dispersion regime, respectively. High-order dispersion is ignored in calculations for simplicity. Microdisk or microsphere SiO_2 resonators generally exhibit large mode volume, which can support multiple transverse co-oscillating intracavity modes.

Leveraging mature dispersion engineering could help to obtain desired normal and anomalous dispersion at the focusing wavelength range [34]. In Eq. (8), $\Re(\eta)$ is the normalized Raman kernel function. H is the Heaviside function. $a = T_0\left(\tau_1^2 + \tau_2^2\right)/\left(\tau_1\tau_2^2\right)$, $b = T_0/\tau_2$, $c = T_0/\tau_1$, where $T_0 = \sqrt{|\beta_2|L/\alpha}$ is the normalization time scale. Variation of T_0 means changing the strength of Raman response function and the physical parameters of resonator including GVD, perimeter and losses [31]. The relationships between $\tau_{1,2}$ and Raman gain parameters are $\tau_1 = 1/\sqrt{\Omega_R^2 - \Gamma_R^2}$, $\tau_2 = 1/\Gamma_R$. The Raman effect is calculated by the convolution theorem, which states $\Re \otimes |\psi|^2 = \mathcal{F}^{-1}\left(\mathcal{F}[\Re] \times \mathcal{F}\left[|\psi|^2\right]\right)$. In Eq. (9), the Raman gain is associated with the imaginary parts of $\mathcal{F}[\Re]$. Technically, Eqs. (6)–(9) can be numerically solved by the Runge-Kutta algorithm combined with Fourier transform.

III. RESULTS AND DISCUSSIONS

We first consider the excitation of STLS in the normal GVD regime. The primary dark pulse can be generated from a modulated pump by means of the conventional frequency scan method, which is widely used for bright soliton generation [35–37]. Figure 2 depicts the spatiotemporal evolution process of the primary dark pulse (blue curve) and the STLS (red curve). Intracavity energy gradually accumulates when linearly increasing the detuning, then the primary dark pulse forms with a step feature at $\zeta = 1000$ shown in Fig. 2(a). The pulse width decreases with continuous increase of detuning between $\zeta = 1000$ and 2700, while the peak power of dark pulse continues to enhance (see the Supplemental Material for more details [38]). A second step feature occurs at $\zeta = 2750$ indicating the emission of the SLS (marked with white dashed line). Raman gain provides enough energy to compensate for cavity losses, resulting in parametric oscillations. One can obviously see the energy of STLS (red curve) abruptly reaches the maximum and holds at it when the detuning keeps unchanged in the remaining time. More details can
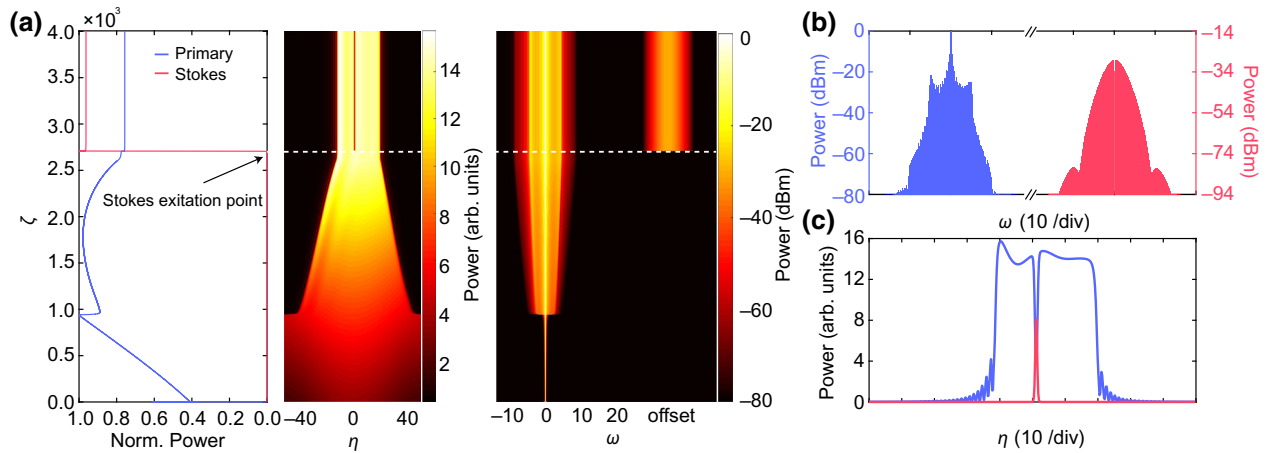
FIG. 2.   Stable primary dark pulse and STLS generation in the normal GVD regime. (a) Left panel, energy traces for primary pulse (blue curve) and STLS (red curve); middle panel, temporal evolution of primary dark pulse; right panel, spectral evolution of dark pulse and STLS. (b) Stable spectra of the primary dark pulse (the blue curve) and the Stokes pulse (the red curve). (c) Final locked pulse profile of the primary dark pulse (the blue curve) and the Stokes pulse. The parameters used are $F = 4.5$, $l = 0.7$, $T_0 = 7$, $d_{p2,s2} = 1$.

be seen from the temporal evolution of dark pulse and STLS [Fig. 2(a)], both of which show stable evolutionary properties. Figure 2(b) depicts the final spectra of the primary dark pulse (the blue curve) and the Stokes pulse (the red curve). In spectral domain, stable dark pulse and STLS are associated with coherent frequency comb generation. The spectrum of the primary comb has two pronounced wings, while the STLS comb exhibits a spectral shape quite different from the traditional platicon in the normal GVD region [39,40]. There is a dip at the top of the primary dark pulse [see Fig. 2(c)] due to the energy transfer of the Raman effect. The primary dark pulse is asymmetric nonlinear object with a pronounced oscillatory tail. STLS shows a bright solitonlike profile reshaped by the Raman gain. The properties of generated pulses, such as width and maximum peak power are strongly affected by the driving field amplitude and the group-velocity dispersion through the characteristic time T_0, as shown in Figs. 3(a)–3(c). The maximum peak power of primary dark slowly increases

with the injected field amplitude as shown in Fig. 3(a), while the FWHM of primary dark pulse increases rapidly with increasing pump power as shown in Fig. 3(b). At a given pump amplitude, the peak power decreases while the FWHM hardly increases with T_0. Figure 3(c) shows the peak power of generated STLS, which apparently increases with both pump amplitude and T_0. It relies on the transfer of pump energy to the Stokes field.

We also observe breathing STLS structures by changing the normalization time scale T_0, which are related to the modification of the SRS response. SRS introduces an additional dependency on the normalization time scale T_0, which is related to the strength of Raman response function and connects to physical parameters of resonator, including GVD, perimeter, and losses. Figure 4 illustrates the spatiotemporal evolution process of the primary breathing dark pulse (blue curve) and the breathing STLS (red curve). The tuning method is the same as that used in Fig. 1 while with larger $T_0 = 10$ fs. The primary dark pulse forms
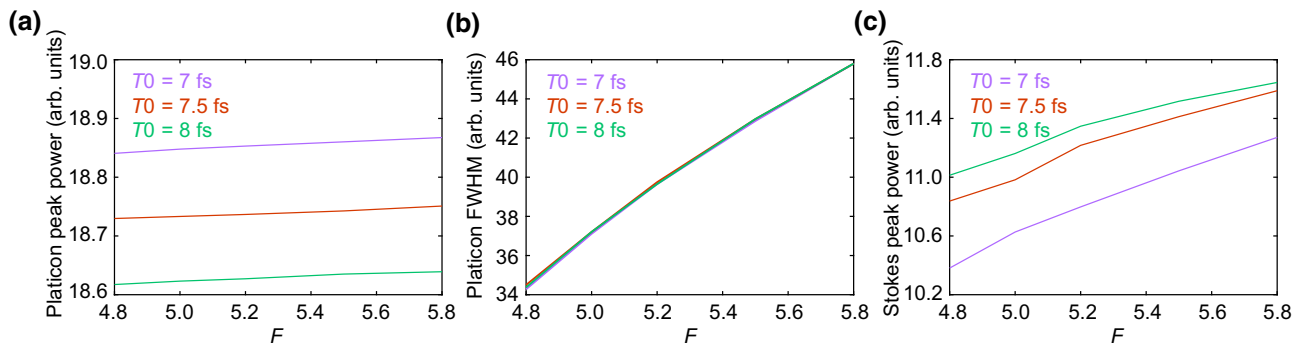

FIG. 3.   Features of the primary and Stokes fields with different pump amplitude and T_0. (a) The maximum peak power and (b) the FWHM of primary dark pulse, (c) the peak power of the STLS as a function of driven field amplitude.
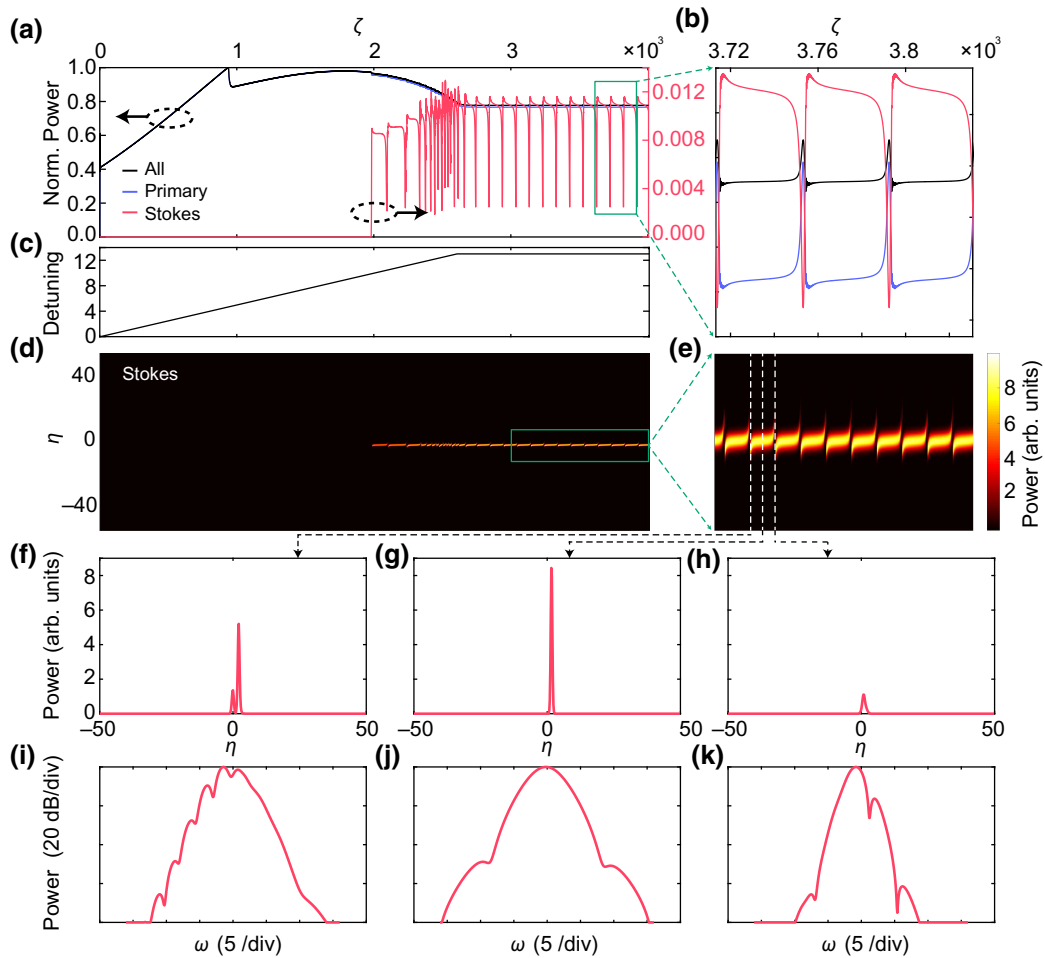
FIG. 4.   Breathing primary dark pulse and STLS generation. (a) Energy traces for primary pulse (blue curve), STLS (red curve), and total intracavity energy (black curve). (b) Enlargement of energy trace of the rectangular region in (a). (c) The detuning is linearly tuned from -0.1 to 13 with a step of 0.02 and held at 13 for stable evolution. (d) Temporal evolution of breathing STLS. (e) Enlargement of the diagram of the rectangular region in (d). (f)–(h) Temporal profile of the Stokes pulse corresponding to the location marked with the white dashed curve. (i)–(k) Spectra of the Stokes pulse in (f)–(h). The detuning is linearly tuned from -0.1 to 13 with a step of 0.02 and held at 13 for stable evolution. The parameters used are $F = 4.5$, $l = 0.7$, $T_0 = 10$, $d_{p2,s2} = 1$.

with a step feature at $\zeta = 900$ shown in Fig. 4(a) (blue curve). The energy accumulates with continuous increase of detuning between $\zeta = 900$ and 1950. A second step feature occurs at $\zeta = 2000$ indicating the emission of the SLS. The energy trace presents periodical oscillation after $\zeta = 2500$ [see Figs. 4(a) and 4(b)], indicating the unstable energy transfer between two pulses. STLS directly becomes the breathing state once reaching the threshold power. The detuning is linearly tuned from -0.1 to 13 with a step of 0.02 and held at 13 for stable evolution, as shown in Fig. 4(c). Figure 4(d) illustrates the temporal evolution of breathing STLS with an enlarged diagram of the rectangular region in Fig. 4(d). Figures 4(f)–4(h) give temporal profiles of the Stokes pulse corresponding to the location marked with white dashed curve with their spectra shown in Figs. 4(i)–4(k). Such a phenomenon can be understood as the following steps: (i) power

accumulation in the primary platicon, (ii) power transfer from the primary platicon to the STLS, and (iii) power dissipation in the STLS. Raman-induced breather platicon has been numerically predicted [41], in which the energy exchange between the pump and the Stokes fields occurs in the same mode. Dark soliton breathers in the normal GVD regime have also been experimentally demonstrated [6], the dynamics of which are dominated by the Kerr effect. However, the breathing STLS observed here is induced by the energy transfer between pump field and the Stokes field, which is quite different from the previously reported dark soliton breathers. One can observe breathing structures by changing pump strength and linear detuning when T_0 is in the range of 3–30 fs. The breathing phenomenon appears at different pump power and laser detuning with a given T_0. Variation of T_0 means changing the physical parameters of resonator, including second-order
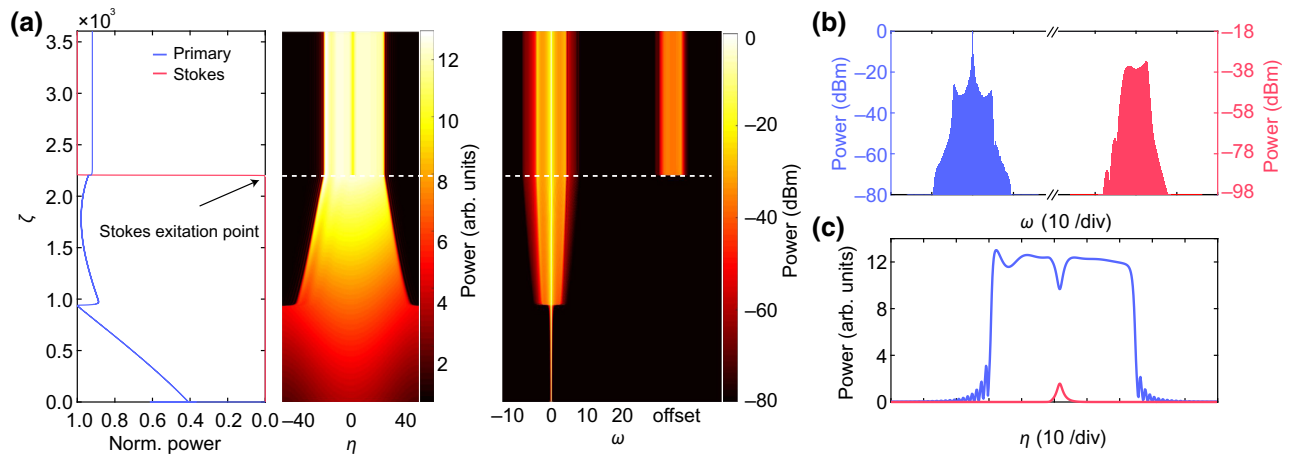
FIG. 5. Stable primary dark pulse and STLS generation in the anomalous GVD regime.(a) Left panel, energy traces for primary pulse (blue curve) and STLS (red curve); middle panel, temporal evolution of primary dark pulse; right panel, spectral evolution of dark pulse and STLS. (b) Stable spectra of the primary dark pulse (the blue curve) and the Stokes pulse (the red curve). (c) Final locked pulse profile of the primary dark pulse (the blue curve) and the Stokes pulse. The parameters used are $F = 4.5$, $l = 0.7$, $T_0 = 7$, $d_{p2} = 1$, $d_{s2} = -1$.

dispersion, cavity total length, and linear losses. So the breathing dynamics is also closely related to microcavity parameters.

Regarding the STLS excitation in the anomalous dispersion regime, similar phenomena can be observed as shown in Fig. 5. In this case, primary platicon is still first generated by pump modulation in the normal GVD, while the Stokes pulse is located at the anomalous GVD region. Intriguingly, the dynamic process is similar to the case in the normal dispersion (shown in Fig. 2). The final spectrum [Fig. 5(b)] and temporal profile [Fig. 5(c)] are quite different. The peak power of the STLS is much smaller than that of the case in Fig. 2(c), indicating a lower conversion efficiency in the anomalous GVD region. The possibility of excitation of the hybrid dark pulse-STLS complexes provides deep insight into the complex dynamics of the nonlinear processes in dissipative Kerr resonators, if the pump and the Stokes modes have alternating signs of the GVD coefficient. These findings could be used to develop and generate microresonator-based microcomb sources with better performance. In the prospective view, such Stokes-localized structures could not only facilitate microcomb-based sensor with high chemical selectivity and high sensitivity, but also leverage applications, including radio-signal generators, frequency modulators, and spatial range finders.

IV. CONCLUSIONS

In summary, we theoretically demonstrate the possibility of STLS excitation and the associated nonlinear dynamics in Kerr resonators with a modulated pump in the normal GVD regime. The hybrid platicon-Stokes complexes are possible whether the Stokes modes have alternating

or identical signs of the GVD coefficient regarding to the primary platicon field. Breathing dynamics and the feature of generated STLS influenced by SRS effect are also investigated in detail. Generation of different types of STLSs represent another pulse-trapping approach in a laser, which may offer an all-optical tool for gas detection with high selectivity and sensitivity. From a practical viewpoint, dispersion engineering could also permit a STLS to form within the same mode family as the primary pulse. Moreover, realizing noncavity-based STLS with a pulse seed is also possible in an appropriately phase-matched multimode waveguide (optical fiber or monolithic).

[1] O. Descalzi, M. Clerc, S. Residori, and G. Assanto, *Localized States in Physics: Solitons and Patterns* (Springer Science & Business Media, Berlin, 2011).

[2] N. Akhmediev, Dissipative solitons/ed. by Akhmediev N., Ankiewicz A, Lecture Notes in Physics. SpringerVerlag **661**, 12005.

[3] Y. Wang, M. Anderson, S. Coen, S. G. Murdoch, and M. Erkintalo, Stimulated Raman Scattering Imposes Fundamental Limits to the Duration and Bandwidth of Temporal Cavity Solitons, Phys. Rev. Lett. **120**, 053902 (2018).

[4] Z. Lu, W. Wang, W. Zhang, S. T. Chu, B. E. Little, M. Liu, L. Wang, C.-L. Zou, C.-H. Dong, B. Zhao, and W. Zhao,

Deterministic generation and switching of dissipative Kerr soliton in a thermally controlled micro-resonator, AIP Adv. **9**, 25314 (2019).

[5] E. Nazemosadat, A. Fülüp, Óskar B. Helgason, P.-H. Wang, Y. Xuan, D. E. Leaird, M. Qi, E. Silvestre, A. M. Weiner, and V. Torres-Company, Switching dynamics of dark-pulse Kerr frequency comb states in optical microresonators, Phys. Rev. A **103**, 13513 (2021).

[6] C. Bao, Y. Xuan, C. Wang, A. Fülöp, D. E. Leaird, V. Torres-Company, M. Qi, and A. M. Weiner, Observation of Breathing Dark Pulses in Normal Dispersion Optical Microresonators, Phys. Rev. Lett. **121**, 257401 (2018).

[7] M. H. Anderson, W. Weng, G. Lihachev, A. Tikan, J. Liu, and T. J. Kippenberg, Zero dispersion Kerr solitons in optical microresonators, Nat. Commun. **13**, 1 (2022).

[8] X. Liu, Z. Gong, A. W. Bruch, J. B. Surya, J. Lu, and H. X. Tang, Aluminum nitride nanophotonics for beyond-octave soliton microcomb generation and self-referencing, Nat. Commun. **12**, 1 (2021).

[9] T. C. Briles, S.-P. Yu, T. E. Drake, J. R. Stone, and S. B. Papp, Generating Octave-Bandwidth Soliton Frequency Combs with Compact Low-Power Semiconductor Lasers, Phys. Rev. Appl. **14**, 014006 (2020).

[10] E. Obrzud, M. Rainer, A. Harutyunyan, M. H. Anderson, J. Liu, M. Geiselmann, B. Chazelas, S. Kundermann, S. Lecomte, M. Cecconi, A. Ghedina, E. Molinari, F. Pepe, F. Wildi, F. Bouchy, T. J. Kippenberg, and T. Herr, A microphotonic astrocomb, Nat. Photon. **13**, 31 (2019).

[11] M.-G. Suh, X. Yi, Y.-H. Lai, S. Leifer, I. S. Grudinin, G. Vasisht, E. C. Martin, M. P. Fitzgerald, G. Doppmann, J. Wang, D. Mawet, S. B. Papp, S. A. Diddams, C. Beichman, and K. Vahala, Searching for exoplanets using a microresonator astrocomb, Nat. Photon. **13**, 25 (2019).

[12] J. Riemensberger, A. Lukashchuk, M. Karpov, W. Weng, E. Lucas, J. Liu, and T. J. Kippenberg, Massively parallel coherent laser ranging using a soliton microcomb, Nature **581**, 164 (2020).

[13] P. Trocha, M. Karpov, D. Ganin, M. Pfeiffer, A. Kordts, S. Wolf, J. Krockenberger, P. Marin-Palomo, C. Weimann, S. Randel, W. Freude, T. Kippenberg, and C. Koos, Ultrafast optical ranging using microresonator soliton frequency combs, Science **359**, 887 (2018).

[14] J. Wang, Z. Lu, W. Wang, F. Zhang, J. Chen, Y. Wang, J. Zheng, S. T. Chu, W. Zhao, B. E. Little, X. Qu, and W. Zhang, Long-distance ranging with high precision using a soliton microcomb, Photo. Res. **8**, 1964 (2020).

[15] E. S. Lamb, D. R. Carlson, D. D. Hickstein, J. R. Stone, S. A. Diddams, and S. B. Papp, Optical-Frequency Measurements with a Kerr Microcomb and Photonic-Chip Supercontinuum, Phys. Rev. Appl. **9**, 024030 (2018).

[16] M. Yu, Y. Okawachi, A. G. Griffith, N. Picqué, M. Lipson, and A. L. Gaeta, Silicon-chip-based mid-infrared dual-comb spectroscopy, Nat. Commun. **9**, 1869 (2018).

[17] L. Stern, J. R. Stone, S. Kang, D. C. Cole, M.-G. Suh, C. Fredrick, Z. Newman, K. Vahala, J. Kitching, S. A. Diddams, and S. B. Papp, Direct Kerr frequency comb atomic spectroscopy and stabilization, Sci. Adv. **6**, eaax6230 (2020).

[18] M.-G. Suh, Q.-F. Yang, K. Y. Yang, X. Yi, and K. J. Vahala, Microresonator soliton dual-comb spectroscopy, Science **354**, 600 (2016).

[19] W. Weng, J. He, A. Kaszubowska-Anandarajah, P. M. Anandarajah, and T. J. Kippenberg, Microresonator Dissipative Kerr Solitons Synchronized to an Optoelectronic Oscillator, Phys. Rev. Appl. **17**, 024030 (2022).

[20] M. Karpov, H. Guo, A. Kordts, V. Brasch, M. H. Pfeiffer, M. Zervas, M. Geiselmann, and T. J. Kippenberg, Raman Self-Frequency Shift of Dissipative Kerr Solitons in an Optical Microresonator, Phys. Rev. Lett. **116**, 103902 (2016).

[21] C. Bao, Y. Xuan, C. Wang, J. A. Jaramillo-Villegas, D. E. Leaird, M. Qi, and A. M. Weiner, Soliton repetition rate in a silicon-nitride microresonator, Opt. Lett. **42**, 759 (2017).

[22] X. Yi, Q.-F. Yang, K. Y. Yang, and K. Vahala, Theory and measurement of the soliton self-frequency shift and efficiency in optical microcavities, Opt. Lett. **41**, 3419 (2016).

[23] Y. He, Q.-F. Yang, J. Ling, R. Luo, H. Liang, M. Li, B. Shen, H. Wang, K. Vahala, and Q. Lin, Self-starting bi-chromatic LiNbO$_3$ soliton microcomb, Optica **6**, 1138 (2019).

[24] S. Yao, Z. Wei, Y. Guo, L. Zhang, J. Wang, J. Yan, C. Bao, and C. Yang, Self-frequency shift of AlN-on-sapphire Kerr solitons, Opt. Lett. **46**, 5312 (2021).

[25] S. Spillane, T. Kippenberg, and K. Vahala, Ultralow-threshold Raman laser using a spherical dielectric microcavity, Nature **415**, 621 (2002).

[26] Q.-F. Yang, X. Yi, K. Y. Yang, and K. Vahala, Stokes solitons in optical microcavities, Nat. Phys. **13**, 53 (2017).

[27] T. Tan, Z. Yuan, H. Zhang, G. Yan, S. Zhou, N. An, B. Peng, G. Soavi, Y. Rao, and B. Yao, Multispecies and individual gas molecule detection using Stokes solitons in a graphene over-modal microresonator, Nat. Commun. **12**, 1 (2021).

[28] Y. Okawachi, M. Yu, V. Venkataraman, P. M. Latawiec, A. G. Griffith, M. Lipson, M. Lončar, and A. L. Gaeta, Competition between Raman and Kerr effects in microresonator comb generation, Opt. Lett. **42**, 2786 (2017).

[29] A. Cherenkov, N. Kondratiev, V. Lobanov, A. Shitikov, D. Skryabin, and M. Gorodetsky, Raman-Kerr frequency combs in microresonators with normal dispersion, Opt. Express **25**, 31148 (2017).

[30] M. G. Clerc, S. Coulibaly, and M. Tlidi, Time-delayed nonlocal response inducing traveling temporal localized structures, Phys. Rev. Res. **2**, 013024 (2020).

[31] P. Parra-Rivas, S. Coulibaly, M. Clerc, and M. Tlidi, Influence of stimulated Raman scattering on Kerr domain walls and localized structures, Phys. Rev. A **103**, 013507 (2021).

[32] G. P. Agrawal, in *Nonlinear Science at the Dawn of the 21st Century* (Springer, 2000), p. 195.

[33] H. Guo, M. Karpov, E. Lucas, A. Kordts, M. H. P. Pfeiffer, V. Brasch, G. Lihachev, V. E. Lobanov, M. L. Gorodetsky, and T. J. Kippenberg, Universal dynamics and deterministic switching of dissipative Kerr solitons in optical microresonators, Nat. Phys. **13**, 94 (2017).

[34] Y. Okawachi, M. R. E. Lamont, K. Luke, D. O. Carvalho, M. Yu, M. Lipson, and A. L. Gaeta, Bandwidth shaping of microresonator-based frequency combs via dispersion engineering, Opt. Lett. **39**, 3535 (2014).

[35] T. Herr, V. Brasch, J. D. Jost, C. Y. Wang, N. M. Kondratiev, M. L. Gorodetsky, and T. J. Kippenberg, Temporal solitons in optical microresonators, Nat. Photon. **8,** 145 (2014).

[36] Z. Lu, H.-J. Chen, W. Wang, L. Yao, Y. Wang, Y. Yu, B. Little, S. Chu, Q. Gong, W. Zhao, X. Yi, X. Yun-Feng, and W. Zhang, Synthesized soliton crystals, Nat. Commun. **12,** 1 (2021).

[37] D. C. Cole, J. R. Stone, M. Erkintalo, K. Y. Yang, X. Yi, K. J. Vahala, and S. B. Papp, Kerr-microresonator solitons from a chirped background, Optica **5,** 1304 (2018).

[38] See Supplemental Material at http://link.aps.org/supplemental/10.1103/PhysRevApplied.18.044028 for simulation animations of stable STLS generation in the normal, anomalous dispersion, as well as breathing STLS generation in the normal dispersion regime.

[39] M. Liu, W. Shi, Q. Sun, H. Huang, Z. Lu, Y. Wang, Y. Cai, C. Wang, Y. Li, and W. Zhao, Free carrier induced dark pulse generation in microresonators, Opt. Lett. **46,** 4462 (2021).

[40] J. Lottes, G. Biondini, and S. Trillo, Excitation of switching waves in normally dispersive Kerr cavities., Opt. Lett. **46,** 2481 (2021).

[41] S. Yao, C. Bao, P. Wang, and C. Yang, Generation of stable and breathing flat-top solitons via Raman assisted four wave mixing in microresonators, Phys. Rev. A **101,** 023833 (2020).